

# Dealloyed Pt<sub>2</sub>Os nanoparticles for enhanced oxygen reduction reaction in acidic electrolytes

Yi-Juei Lee<sup>a</sup>, Yu-Chi Hsieh<sup>a</sup>, Ho-Cheng Tsai<sup>b</sup>, I-Te Lu<sup>a</sup>, Yue-Han Wu<sup>a</sup>, Ted H. Yu<sup>b,c</sup>, Jyh-Fu Lee<sup>d</sup>, Boris V. Merinov<sup>b</sup>, William A. Goddard III<sup>b</sup>, Pu-Wei Wu<sup>a,\*</sup>

<sup>a</sup> Department of Materials Science and Engineering, National Chiao Tung University, Hsinchu 300, Taiwan, ROC

<sup>b</sup> Materials and Process Simulation Center, MC 139-74 California Institute of Technology, Pasadena, CA 91125, USA

<sup>c</sup> Department of Chemical Engineering, California State University, Long Beach, Long Beach, CA 90840, USA

<sup>d</sup> National Synchrotron Radiation Research Center, Hsinchu 300, Taiwan, ROC

## ARTICLE INFO

### Article history:

Received 6 August 2013

Received in revised form

20 November 2013

Accepted 3 January 2014

Available online 10 January 2014

### Keywords:

Oxygen reduction reaction

Platinum

Osmium

Dealloying process

Quantum mechanics

## ABSTRACT

Carbon-supported Pt<sub>2</sub>Os (Pt<sub>2</sub>Os/C) nanoparticles in 3.55 nm sizes are synthesized from a wet chemical reflux process. Subsequently, the Pt<sub>2</sub>Os/C undergoes a dealloying treatment in which multiple cyclic voltammetric scans are imposed to dissolve the Os atoms selectively from the surface of the Pt<sub>2</sub>Os nanoparticles. X-ray diffraction signals from the dealloyed sample (DA-Pt<sub>2</sub>Os/C) indicate a fcc phase and composition analysis suggests Pt<sub>4</sub>Os. Line scans from the scanning transmission electron microscope confirm that the surface of Pt<sub>4</sub>Os is depleted with the Os atoms. This agrees with our quantum mechanics (Density Functional theory) calculations, which predict for the Pt<sub>3</sub>Os composition that the surface skin layer is pure Pt. The DA-Pt<sub>2</sub>Os/C shows impressive electrocatalytic behaviors (0.29 mA µg<sub>Pt</sub><sup>-1</sup> in mass activity and 1.03 mA cm<sub>Pt</sub><sup>-2</sup> in specific activity) for the oxygen reduction reaction (ORR) in oxygen-saturated 0.1 M aqueous HClO<sub>4</sub> solution, as compared to those of commercially available Pt/C and as-synthesized Pt<sub>2</sub>Os/C. In stability test, the DA-Pt<sub>2</sub>Os/C demonstrates a better retention of ORR activities and a smaller loss of electrochemical active surface area. We verify experimentally that a four-electron step is responsible for the ORR process occurring on the DA-Pt<sub>2</sub>Os/C.

© 2014 Elsevier B.V. All rights reserved.

## 1. Introduction

Hydrogen-based fuel cells are considered as one of the clean energy alternatives to reduce carbon dioxide emissions by replacing conventional energy generation means using fossil fuels [1,2]. During the operation of fuel cells, the hydrogen is oxidized at the anode and the oxygen is reduced at the cathode. Between them, the oxygen reduction reaction (ORR) is the rate-determining step because the oxygen molecules are slow to split and react at the cathode/electrolyte interface [3–7]. To date, many materials have been explored for the ORR activities in acidic electrolytes. For example, metals like Pt and Pd, organometallic complexes like cobalt phthalocyanines (CoPc), cobalt-polypyrrole–carbon black (Co–PPY–CB) and Fe–N<sub>4</sub>, transition metal oxides like MnO<sub>2</sub> and TiO<sub>x</sub>, as well as chalcogenides like W<sub>11</sub>–Co<sub>43</sub>–Se<sub>46</sub> and Co<sub>3</sub>S<sub>4</sub> have been reported with various results [8–18]. Among them, the Pt has received the most attention in recent years because of its notable ORR activities and chemical stability. So far, Pt in a wide variety of

nanostructures/morphologies have been synthesized and studied for ORR actions [19–24].

The Pt is a noble metal and its cost becomes a serious concern to the commercialization of fuel cells. Therefore, substantial efforts have been devoted to identify secondary elements to alloy with the Pt for cost reduction and possible ORR enhancements. The study of binary PtM (M=Cu, Ni, Co, Fe, etc.) has produced significant results and the Pt<sub>3</sub>Ni has emerged as the leading candidate as an ORR electrocatalyst in acidic electrolytes [7,25–35]. It is rationalized that for the (1 1 1) plane of Pt<sub>3</sub>Ni, the unique surface geometry and electronic structure lead to the impressive ORR activity and stability. Another approach to enhance the ORR activity is to synthesize electrocatalysts in distinct core–shell nanostructures. In this way, the inexpensive element constitutes the core whereas the expensive noble one occupies the shell and is responsible for the ORR action. This can be realized by a copper under potential deposition technique in which the Pt is deposited via a galvanic displacement reaction to form a mono-layered film for extremely low Pt utilization rate [21,36,37]. An alternative route to fabricate desirable core–shell nanostructures is the dealloying method. The dealloying process entails an electrochemical step to induce a selective dissolution of less noble element from a binary Pt-based electrocatalyst and consequently, produces a surface enriched with the

\* Corresponding author at: Corresponding author. Tel.: +886 3 5131227; fax: +886 3 5724727.

E-mail addresses: [ppwu@mail.nctu.edu.tw](mailto:ppwu@mail.nctu.edu.tw), [puweiwu@yahoo.com](mailto:puweiwu@yahoo.com) (P.-W. Wu).

Pt atoms. According to Strasser et al., the dealloyed nanocatalysts reveal a compressive strain in the Pt-enriched shell that modifies the d-band structure of the Pt atoms and therefore, the electrocatalytic activities for ORR are significantly enhanced [38]. To date, many dealloyed nanoparticles including binary Pt–Cu, Pt–Co, and Pt–Ni, and ternary Pt–Cu–Co, PtNi<sub>3</sub>M (M=Cu, Co, Fe, Cr) have been synthesized and evaluated for ORR activities [39–45].

Previously, binary Pt<sub>x</sub>Os<sub>y</sub> nanoparticles have been studied as promising electrocatalysts for methanol oxidation reaction (MOR) in direct methanol fuel cells. It is because both experimental results and quantum mechanics (QM) calculations indicated active roles of Os to facilitate nearby Pt for MOR actions [46–49]. Kua and Goddard used QM to show that Os can activate both the CH bonds and OH bonds of methanol whereas otherwise an alloy is required, for example activation of CH bonds by Pt and OH bonds by Ru [46]. In addition, Zhu et al. reported that the Pt–Os electrode exhibited an improved MOR activity promoted by the adsorbed OH species, but the formation of OsO<sub>2</sub> might be detrimental [48]. In addition, the adsorption and oxidation of CO on the Pt<sub>x</sub>Os<sub>y</sub> had been investigated by Liu et al. in which the threshold potential for CO oxidation on the Pt–Os (4:1 in molar ratio) was nearly identical to that of Pt–Ru (4:1 in molar ratio) [50]. Moreover, according to Kim et al., the oxidation of CO on the Os-modified Pt (111) plane was accelerated because the Os atoms increased the mobility of the adsorbed CO by altering the electronic structure of the Pt atoms, and thus minimized the CO-poisoning effect [51].

The oxyphilic nature of the Os atoms is a desirable attribute for ORR action. A QM simulation by Yu et al. suggested that the Pt<sub>3</sub>Os alloy tended to form a segregated surface structure (the 1st layer is 100% Pt, the 2nd layer is 50% Pt and 50% Os, and the 3rd layer is 75% Pt and 25% Os) [52]. It is noted that the Pt-skin surface is expected to enhance the ORR activity by reducing the energy barrier for ORR steps [53]. This has been confirmed in a recent report in which a Pt<sub>0.8</sub>Os<sub>0.2</sub> monolayer deposited on a Pd (111) surface demonstrated a rather impressive ORR activity because the presence of Os atoms engendered a weaker affinity for the adsorbed oxygen and consequently, a reduction in the OH adsorption on the active Pt sites [54]. Therefore, we rationalized that the alloyed Pt<sub>x</sub>Os<sub>y</sub> nanoparticles might be promising electrocatalysts for ORR in acidic electrolytes.

In this work, we demonstrated the synthesis of Pt<sub>2</sub>Os nanoparticles and employed a dealloying treatment to render a quasi core–shell Os@Pt nanostructure. Extensive material characterization was carried out to understand structural/compositional evolution during the dealloying treatments. The dealloyed sample was evaluated for ORR activities and life time performance, and the results were compared with commercially available Pt nanoparticles. In addition, we performed QM calculations of surface segregation on PtOs systems and compared to the experimental results.

## 2. Experimental and computational methods

### 2.1. Pt<sub>2</sub>Os synthesis

Carbon-supported Pt<sub>2</sub>Os nanoparticles were prepared in a chemical reduction route. First, 80 mg of carbon powders (particle size <50 nm, Sigma Aldrich) were suspended in 50 mL of deionized water at 80 °C. Next, 36 mg of H<sub>2</sub>PtCl<sub>6</sub>·6H<sub>2</sub>O (UniRegion Bio-Tech) and 17 mg of K<sub>2</sub>OsCl<sub>6</sub> (Sigma-Aldrich) were dissolved in 50 mL of deionized water (molar ratio of Pt/Os = 2), and the solution was added to the carbon suspension. Subsequently, 21 mg of citric acid was added as a chelating agent. The mixture was stirred for 30 min at 80 °C in an argon flow under reflux to produce a homogeneous suspension. Afterward, 76 mg of NaBH<sub>4</sub> was added serving as a

reducing agent, and the mixture underwent further stirring for 2 h at 80 °C in an argon flow under reflux to ensure the complete reduction of Pt and Os ions, and the formation of Pt<sub>2</sub>Os nanoparticles impregnated on the carbon powders. The as-synthesized sample was labeled as Pt<sub>2</sub>Os/C. Next, the Pt<sub>2</sub>Os/C powders were filtered and washed to remove residual chloride ions. After drying at 25 °C in air for 8 h, a reduction treatment at 250 °C in a hydrogen flow (100% H<sub>2</sub>) was performed for 2 h. The effective metal loading of the Pt<sub>2</sub>Os nanoparticles was 20 wt% of the Pt<sub>2</sub>Os/C sample.

### 2.2. Electrochemical analysis

10 mg of Pt<sub>2</sub>Os/C powders underwent an ultrasonication mixing for 5 min in a solution containing 3 mL of deionized water, 2 mL of ethanol, and 2 μL of 5 wt% Nafion ionomer solution (Sigma-Aldrich) to render an uniform ink dispersion. Subsequently, 15 μL of the ink dispersion was deposited on a glassy-carbon rotation disk electrode (RDE) serving as a working electrode (Pine Research, electrode diameter is 5 mm and the electrode area is 0.1963 cm<sup>2</sup>). To initiate the selective dissolution of Os atoms from the Pt<sub>2</sub>Os nanoparticles, known as a dealloying process, multiple cyclic voltammetry (CV) scans were imposed between –0.2 and 0.8 V at 50 mV s<sup>–1</sup> in a 50 mL deaerated 0.1 M aqueous HClO<sub>4</sub> solution. After the dealloying process, the sample was labeled as DA–Pt<sub>2</sub>Os/C. The coulombic charge associated with the hydrogen underpotential deposition region (–0.2 to 0.2 V vs. Ag/AgCl) was estimated and divided by 210 μC cm<sup>–2</sup> [55,56] to obtain the electrochemical active surface area (ECSA) for the Pt<sub>2</sub>Os/C and DA–Pt<sub>2</sub>Os/C. To explore the electrocatalytic activities for ORR, CV scans between –0.2 and 0.8 V were performed at 10 mV s<sup>–1</sup> in 50 mL of 0.1 M aqueous HClO<sub>4</sub> solution. Prior to the ORR experiments, the HClO<sub>4</sub> aqueous solution was bubbled with oxygen for 30 min to ensure it was fully saturated with the oxygen. Durability tests were performed using CV scans at 50 mV s<sup>–1</sup> between 0.36 and 0.76 V in 50 mL of 0.1 M aqueous HClO<sub>4</sub> solution. The durability test lasted for 10,000 cycles and the electrolyte was exposed to the ambient air throughout the entire cycles. The electrochemical measurements were performed at 25 °C in a three-electrode arrangement using a Solartron 1287A electrochemical interface. A Ag/AgCl and Pt foil (15 cm<sup>2</sup>) were used as the reference and counter electrodes, respectively. The potential for the reversible hydrogen electrode (RHE) was –0.289 V (vs. Ag/AgCl). In our figures, all potentials were plotted against the RHE. Lastly, identical electrochemical tests were performed on commercially available Pt/C (20 wt% Pt on Vulcan XC72R, BASF) for comparison purpose.

### 2.3. Materials characterization

A high-resolution transmission electron microscope (TEM; JEOL JEM3000F) was employed to observe the morphologies, sizes, and distributions of the Pt<sub>2</sub>Os/C and DA–Pt<sub>2</sub>Os/C. The structures and composition profiles of the Pt<sub>2</sub>Os and DA–Pt<sub>2</sub>Os nanoparticles were obtained using a JEOL spherical aberration corrected scanning transmission electron microscope (ARM 200F) with an Oxford energy dispersive spectrometer (EDS) in which the L<sub>α</sub> and M<sub>α</sub> signals from the EDS were recorded to determine the spatial distribution of the Pt and Os atoms in the Pt<sub>2</sub>Os and DA–Pt<sub>2</sub>Os nanoparticles. A scanning electron microscope (SEM; JEOL JSM6500F) and a total reflection X-ray fluorescence spectrometer (TRXF; Bruker S2-PICOFOX) were employed to estimate the atomic ratio of Pt/Os in the Pt<sub>2</sub>Os and DA–Pt<sub>2</sub>Os nanoparticles. The exact Pt amount in our samples was determined using an inductively coupled plasma mass spectrometer (ICP–MS; Agilent 7500ce). An X-ray diffractometer (XRD; Bruker D2 Phaser) equipped with a Cu K $\alpha$  radiation source ( $\lambda = 1.54 \text{ \AA}$ ) was used to

**Table 1**Structural parameters and composition of Pt/C, Pt<sub>2</sub>Os/C, and DA-Pt<sub>2</sub>Os/C electrocatalysts.

Sample	Peak angle ( $2\theta$ )	Lattice constant (Å)	Particle size <sup>a</sup> (nm)	Particle size <sup>b</sup> (nm)	Atomic ratio <sup>c</sup> Pt/Os	Atomic ratio <sup>d</sup> Pt/Os
Pt/C	39.5	3.95	2.26	2.58 ± 1.7	–	–
Pt <sub>2</sub> Os/C	41.01	3.81	3.65	3.55 ± 2	68/32	67/33
DA-Pt <sub>2</sub> Os/C	40.43	3.85	3.7	3.86 ± 1.6	93/7	81/19

<sup>a</sup> Mean particle size calculated from Debye–Scherrer equation on Pt (1 1 1) and Pt<sub>2</sub>Os (2 2 0) planes.<sup>b</sup> Mean particle size observed from TEM images.<sup>c</sup> Atomic ratio determined by TXRF.<sup>d</sup> Atomic ratio determined by SEM–EDS.

identify relevant phases and crystal sizes for both Pt<sub>2</sub>Os/C and DA-Pt<sub>2</sub>Os/C.

The X-ray absorption spectroscopy (XAS) experiments on Pt<sub>2</sub>Os/C and DA-Pt<sub>2</sub>Os/C were performed at beam line of BL01C1 at Taiwan Light Source, National Synchrotron Radiation Research Center (NSRRC), Hsinchu, Taiwan. The measurements were carried out in a fluorescence detection mode at 25 °C. A Pt foil was used as the reference for Pt L<sub>III</sub>-edge spectra. X-ray absorption near edge structure (XANES) data analysis and fitting were processed by an IFEFFIT 1.2.11c data analysis package (Athena). The recorded profile was calibrated by aligning against the reference in each scan. During measurements, multiple spectra for a single absorption edge were collected and averaged to achieve better signal quality. Each raw spectrum was pre-edge subtracted to remove the background and then was normalized with respect to the edge jump. Details in the XAS measurements can be found elsewhere [57].

#### 2.4. Computational methods

The method applied for the surface segregation calculations is similar to that used in our previous study [52]. Periodic QM calculation were carried out with the SeqQuest code [58], which employs Gaussian basis functions at the optimized double zeta plus polarization level, rather than the plane-wave basis often used in periodic systems. We used density functional theory (DFT) with the Perdew–Burke–Ernzerhof (PBE) functional [59] and the generalized gradient approximation (GGA) [60] for exchange correlation. Small core angular-momentum-projected norm-conserving nonlocal effective core potentials (pseudopotentials) [61–64] were employed to replace the core electrons.

To represent the surface we used hexagonal close packed (1 1 1) slabs with a 2 × 2 unit cell for either five or six layers and a 3 × 3 unit cell for four layers which is similar to the approach used in our surface segregation calculations. The results obtained for the different slabs are rather similar. We consider the Pt<sub>3</sub>Os structure represent both the original composition of Pt<sub>4</sub>Os, and the dealloyed composition of a DA-Pt<sub>2</sub>Os sample, whose composition is nearly Pt<sub>4</sub>Os. For the lattice parameter optimization, we assumed the ordered L<sub>1</sub><sub>2</sub> cubic structure with Pt at the center of the face and Os at the corners. The reciprocal space grid was 12 × 12 × 12 for the lattice constant calculation. The optimized lattice constant for Pt<sub>3</sub>Os is 3.94 Å, slightly smaller than 3.98 Å found for pure Pt. For the 5-layer segregation calculation, the top two layers are allowed to relax, but the bottom three layers are fixed. The real space grid density is five points per angstrom while the reciprocal space grid was 5 × 5 × 0 for all the slab calculations. The self consistent field (SCF) and the force convergence criteria were 5 meV and 0.02 eV Å<sup>−1</sup>, respectively.

### 3. Results and discussion

In the literatures, binary Pt<sub>x</sub>Os<sub>y</sub> nanoparticles have been prepared via wet chemical routes such as chemical reduction and electrochemical deposition [48,65]. Due to a notable difference in the redox potentials between the Pt, Os, and their corresponding

ions, the careful control in the formation stage is essential in order to obtain Pt<sub>x</sub>Os<sub>y</sub> nanoparticles with desirable compositions. Our reflux approach enables the synthesis of stoichiometric Pt<sub>2</sub>Os nanoparticles in large quantity. For the dealloying process, so far, techniques including chemical dissolution and electrochemical dissolution have been employed. Between them, the chemical dissolution approach is simple and effective for producing large-quantity of nanoparticles [66]. In contrast, the electrochemical dissolution route entails external stimulus (voltage or current) to selectively remove the active constituent and therefore enables the precise control of dealloying severity (composition and atomic distribution in a binary nanoparticle). In general, the electrochemical dissolution process can be carried out in potentiostatic, galvanostatic, and CV modes. The potentiostatic and galvanostatic modes are often used to produce porous films because the straightforward imposition of voltage or current renders substantial dissolution effect [67,68]. In contrast, the CV scans are adopted primarily to form nanoparticles because the potential sweeps limit the duration at high anodization potentials and allows for the reduction/recovery during the cathodic scans [69,39,70]. It is therefore suggested that for nanoparticles, the CV dealloying treatment is a better approach to form core–shell or quasi-core–shell microstructures.

Fig. 1 displays the TEM images of Pt/C, Pt<sub>2</sub>Os/C, and DA-Pt<sub>2</sub>Os/C, respectively. For both Pt/C and Pt<sub>2</sub>Os/C, uniform distributions of irregularly-shaped nanoparticles with moderate aggregation were observed, and their average sizes were 2.58 ± 1.7 and 3.55 ± 2 nm. The slight increment in sizes and wider distribution for the Pt<sub>2</sub>Os/C over Pt/C were possibly due to the reflux process that allowed for multiple events of nucleation and growth. After the dealloying treatment, the DA-Pt<sub>2</sub>Os/C showed a similar morphology and distribution, and the average size became 3.86 ± 1.6 nm. The details of determining the average nanoparticle sizes are provided in the Supporting Information.

Fig. 2 demonstrates the XRD patterns of Pt/C, Pt<sub>2</sub>Os/C, and DA-Pt<sub>2</sub>Os/C, as well as standard Pt (JCPDS: 88-2343) and Os (JCPDS: 88-1704). For the Pt/C sample, a broad peak between 25° and 30° was attributed to the interference from the carbon support. In addition, the diffraction signals located at 39.6°, 46.2°, and 67.3° were identified as the (1 1 1), (2 0 0), and (2 2 0) peaks of the fcc Pt structure. These diffraction signals revealed characteristic peak-broadening phenomenon because of the finite Pt particle size. We estimated the Pt particle size of 2.3 nm using the Debye–Scherrer equation on the (1 1 1) peak. For the Pt<sub>2</sub>Os/C sample, similar diffraction signals were obtained and they were located at 41°, 47.4°, and 69°, respectively. Because the size of the Os atom (1.35 Å) is smaller than that of Pt (1.39 Å), in Pt<sub>2</sub>Os nanoparticles, the Os atoms were likely to adopt the fcc Pt structure and form a solid solution with the Pt. As a result, the Pt<sub>2</sub>Os diffraction peaks were expected to shift slightly to larger angles, which is consistent with our results. Using the Debye–Scherrer' equation on the (2 2 0) peak, the size of the Pt<sub>2</sub>Os nanoparticle was estimated at 3.65 nm. More discussion on the lattice parameter of Pt<sub>2</sub>Os is provided in the Supporting Information.

According to the binary phase diagram of Pt and Os, a homogeneous solid solution is present when the molar ratio for the Os

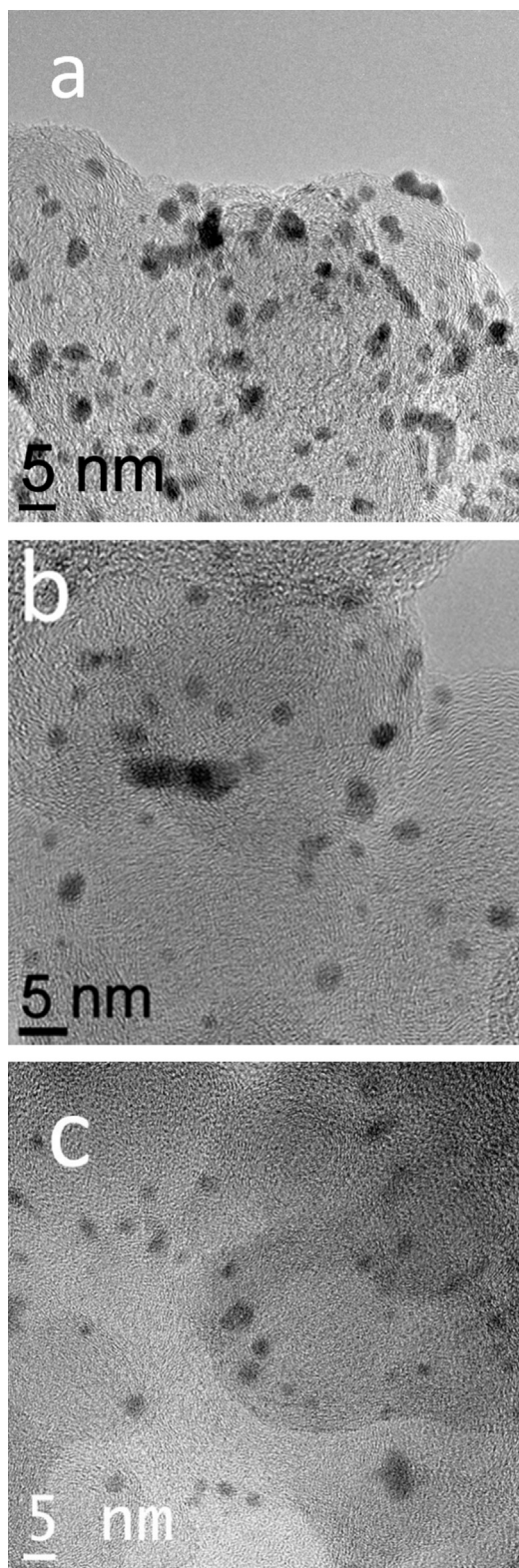


**Fig. 1.** The TEM images of Pt/C, Pt<sub>2</sub>Os/C, and DA–Pt<sub>2</sub>Os/C.

atoms is in the range of 0–20% [48,49]. Above 20%, the Os atoms precipitate out as a hcp phase with limited solubility of Pt. However, in the case of nanoparticles, it has been confirmed that a single fcc phase is still possible with a Pt:Os molar ratio of 1:1.1 [71]. Therefore, we believed that our Pt<sub>2</sub>Os nanoparticles exist as a single fcc phase. The hcp Os phase has characteristic peaks at 38°, 42°,

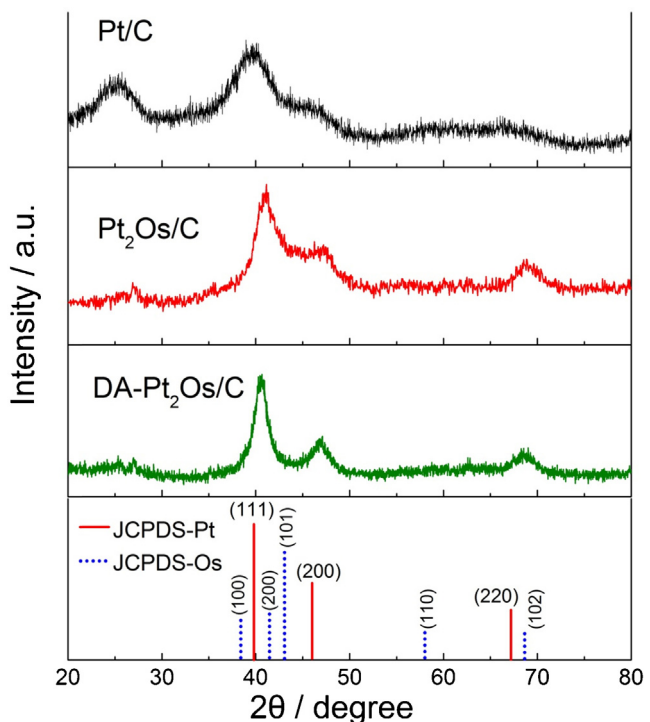


**Fig. 2.** The X-ray diffraction patterns of Pt/C, Pt<sub>2</sub>Os/C, and DA–Pt<sub>2</sub>Os/C, as well as fcc Pt (JCPDS: no. 88-2343) and hcp Os (JCPDS: no. 88-1704).

44°, 58°, and 69° (JCPDS: 88-1704). From the diffraction signals of Pt<sub>2</sub>Os/C, the possibility of minor presence of Os peaks at 42° and 44° cannot be ruled out. However, we did not observe any single-phase Pt and Os nanoparticles from STEM images (to be discussed in Fig. 4) so we could reasonably conclude that the as-synthesized Pt<sub>2</sub>Os is an alloyed nanoparticle. After the dealloying process, the broadened diffraction signals between 41° and 47° became sharpened considerably. After the removal of Os atoms from the surface of the Pt<sub>2</sub>Os nanoparticles, the diffraction peaks indicate Pt-dominant signals from the (111), (200), and (220) planes.

Table 1 lists the particle size of our samples from XRD diffraction signals and TEM images, as well as results from the composition determination. The estimation of nanoparticles sizes using the Debye–Scherrer equation was rather consistent with those from TEM images. In addition, composition analysis from the TXRF and SEM–EDS confirmed that the atomic ratios of Pt/Os were 68/32 and 67/33 for the Pt<sub>2</sub>Os nanoparticles. These values were very close to the stoichiometric ratio of 2:1. The atomic ratio of DA–Pt<sub>2</sub>Os from SEM–EDS was 81/19. This result substantiated our dealloying process to convert the as-synthesized Pt<sub>2</sub>Os into Pt<sub>4</sub>Os. It is noted that the dealloying process removed the Os atoms selectively from the surface of the Pt<sub>2</sub>Os nanoparticles and consequently, the Pt<sub>4</sub>Os should be recognized as the average composition of the dealloyed sample, DA–Pt<sub>2</sub>Os.

Fig. 3 shows the CV curves for Pt<sub>2</sub>Os/C in deaerated 0.1 M aqueous HClO<sub>4</sub> solution at the 3rd, 10th, 50th, and 60th cycles, respectively. For the CV curve of the 3rd cycle, two distinct oxidation signals were observed; one minor peak at 0.7 V and the other strong one starting at 0.85 V. From the previous studies on the Os systems, the oxidation peak at 0.7 V is associated with the oxidation of Os atoms to OsO<sub>2</sub> whereas the oxidation peak of 0.85 V is attributed to the oxidation of OsO<sub>2</sub> to OsO<sub>4</sub> [72,73]. According to Greidan et al. [74], in an aqueous solution the OsO<sub>2</sub> is insoluble but the OsO<sub>4</sub> can be dissolved moderately. Therefore, we observed a relatively strong oxidation current at 0.85 V in the anodic scan but a subdued reduction current at 0.3–0.5 V in the cathodic scan because

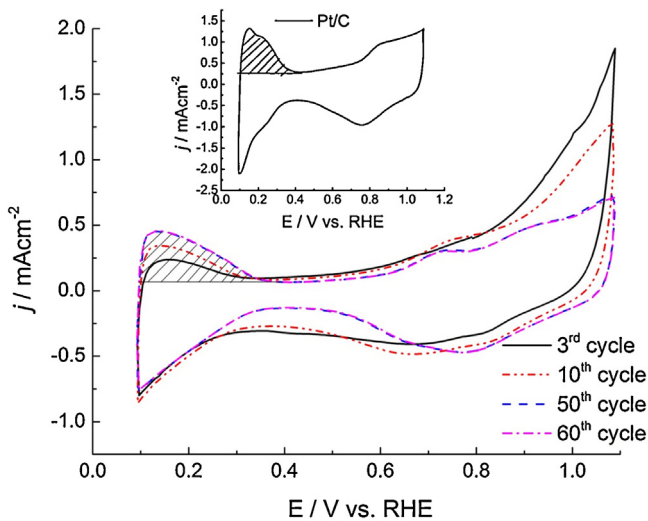


**Fig. 3.** The CV curves of Pt<sub>2</sub>Os/C undergoing the dealloying treatment of 3rd, 10th, 50th, and 60th cycles, respectively. The electrolyte was deaerated 0.1 M aqueous HClO<sub>4</sub> solution and the scan rate was 50 mV s<sup>-1</sup>. The highlighted areas were used to estimate the ECSA values. Inset is the CV curve for the Pt/C for ECSA determination.

most of the OsO<sub>4</sub> was dissolved in the electrolyte during the anodic scan and thus was unable to participate in the subsequent reduction process in the cathodic scan. It is noted that our results of broad reduction currents are consistent with a previous report by Rhee et al. in which the Os nanoislands were spontaneously deposited and electrochemically stripped from a Pt (111) single crystal substrate [75]. It is noted that the Pt oxidation also occurred at 0.8 V and the corresponding reduction peak was located at 0.75 V during the cathodic scan (as shown in the inset of Fig. 3). Therefore, in our case at voltage above 0.85 V, the oxidation of OsO<sub>2</sub> to OsO<sub>4</sub>, and the oxidation of Pt were both responsible for the anodic currents.

Upon further cycling, the currents associated with the Os oxidation and reduction were progressively reduced. This confirmed that the Os atoms in the Pt<sub>2</sub>Os nanoparticles were selectively removed resulting in a surface gradually enriched with the Pt atoms. This dealloying process was effective until the 50th CV as further CV cycles engendered a negligible difference in the CV curves. At this stage, the remaining Os atoms exposing to the electrolyte were rather limited, and the out-diffusion of the Os atoms from the core was considered unlikely due to the relatively low working temperature (25 °C) and short dealloying time (33 min). With the steady loss of Os atoms from the Pt<sub>2</sub>Os nanoparticles, more Pt atoms were exposed to the electrolyte and consequently, a larger ECSA was obtained. The areas used to estimate the ECSA were highlighted

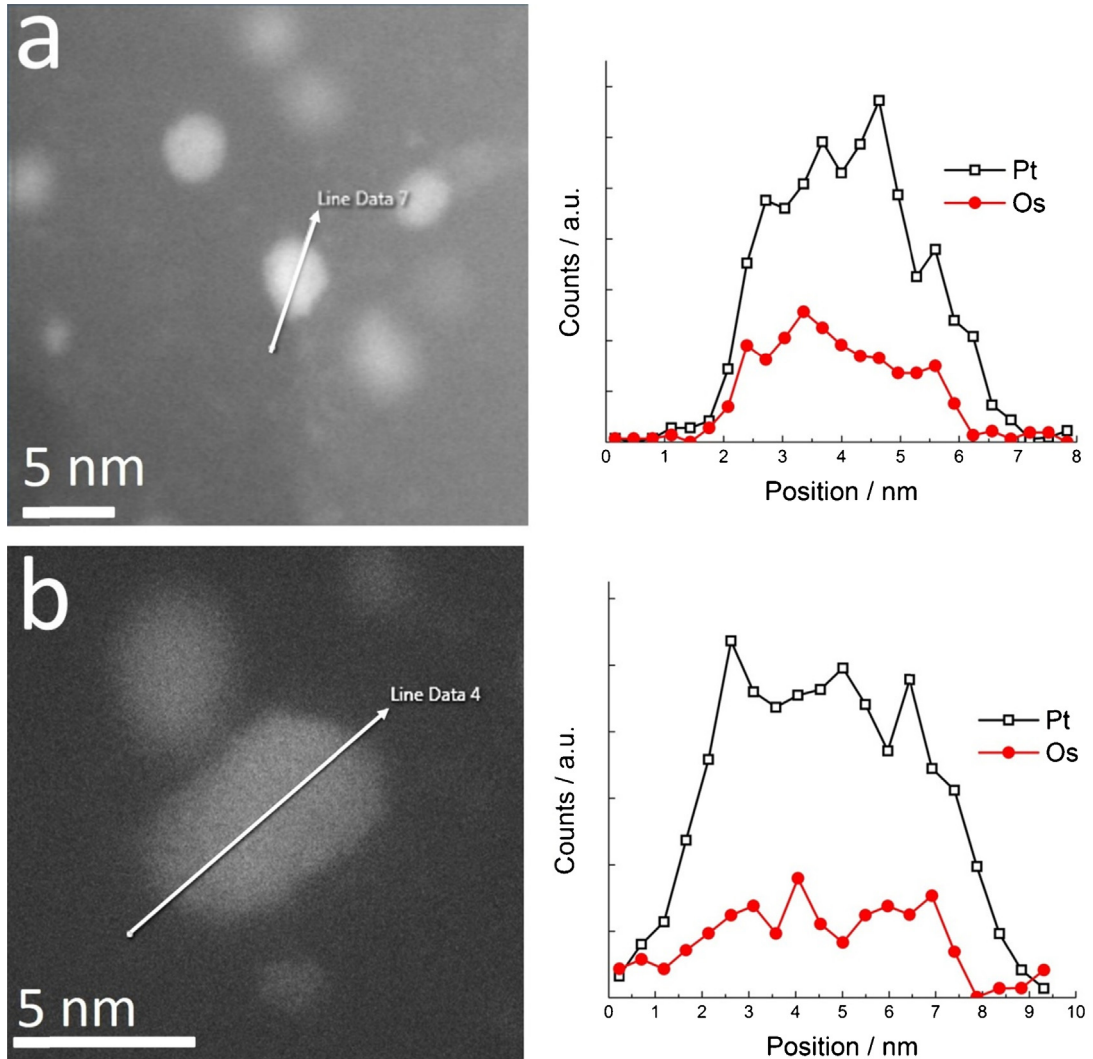


**Fig. 4.** The STEM images and EDS line-scans of (a) Pt<sub>2</sub>Os and (b) DA-Pt<sub>2</sub>Os nanoparticles.

at a potential window of 0.09 and 0.35 V, and their respective values were 0.32, 0.66, and  $1.13 \text{ cm}_{\text{Pt}}^{-2}$  for the 3rd, 10th, and 50th cycle, respectively. These increasing ECSA values substantiated that the de-alloying process was achieved successfully that rendered a greater number of Pt atoms on the surface. Because the CV profiles after 50 cycles revealed a negligible variation, we selected the 50th cycle as the standard de-alloying treatment for following tests.

The elemental profiles of Pt and Os in the Pt<sub>2</sub>Os and DA-Pt<sub>2</sub>Os nanoparticles were obtained by the STEM-EDS measurements with a probe size of about 1.5 Å. Fig. 4a exhibits a STEM image and the corresponding line-scan profile across a Pt<sub>2</sub>Os nanoparticle in 4.5 nm size. The result suggested an alloy state for the as-synthesized Pt<sub>2</sub>Os nanoparticles. Fig. 4b shows a STEM image and the line-scan profile of a DA-Pt<sub>2</sub>Os nanoparticle of 7 nm in diameter. Apparently, the Os atoms residing on the surface regime were mostly removed and the DA-Pt<sub>2</sub>Os (Pt<sub>4</sub>Os) revealed a quasi-core–shell structure in which the core retained some Os atoms whereas the shell was occupied by the Pt atoms exclusively.

The XANES spectra for the standard Pt foil, Pt<sub>2</sub>Os, and DA-Pt<sub>2</sub>Os are displayed in Fig. 5. The absorption intensity of the L<sub>III</sub>-edge, known as the white line intensity, depends on the electronic transition probability of 2p<sub>3/2</sub> to 5d. In general, a sample with a lower occupancy of the 5d electronic states indicates a higher oxidation number, which leads to a greater white line intensity. The as-prepared Pt<sub>2</sub>Os underwent a hydrogen treatment before the XAS measurements, therefore, the higher white line intensity of Pt atom was not caused by the formation of surface Pt oxide. Instead, it was attributed to the interaction between the Pt and Os atoms. This result supports our argument that the as-synthesized Pt<sub>2</sub>Os was in an alloyed state. After the de-alloying process, the white light intensity of the DA-Pt<sub>2</sub>Os was reduced slightly just below that

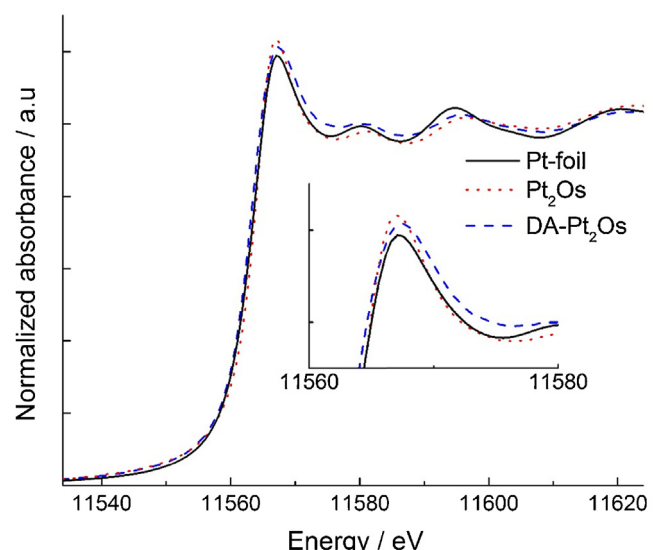


Fig. 5. The >normalized Pt L<sub>III</sub>-edge XANES spectra for bulk Pt, Pt<sub>2</sub>Os, and DA-Pt<sub>2</sub>Os.

of Pt<sub>2</sub>Os. In the de-alloying process in which the Os atoms were selectively removed from the surface of Pt<sub>2</sub>Os nanoparticles, the oxidation state of Pt atoms moved closer to that of bulk Pt. Nevertheless, it is apparent that the DA-Pt<sub>2</sub>Os exhibited a higher white line intensity as opposed to that of Pt, suggesting that the Os atoms at the core were still intact.

The extended X-ray absorption fine structure (EXAFS) is known to detect the segregation phenomenon in binary nanoparticles

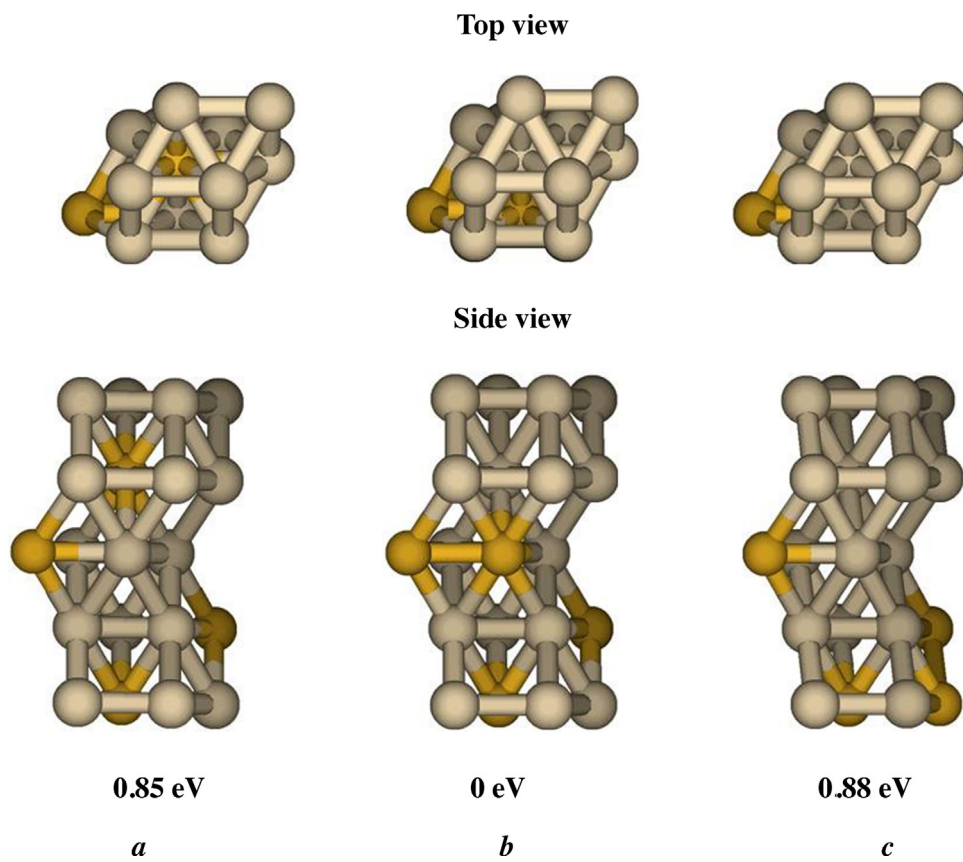


Fig. 6. The surface segregation models for five layers of DA-Pt<sub>2</sub>Os (Pt<sub>4</sub>Os) electrocatalysts. a—The uniformly distributed structure, b—the segregated structure with Os enriched in the third layer, and c—the segregated structure with Os enriched in the bottom layer. The energies are relative to the energy of the most stable structure b,  $-48849.55 \text{ eV}$ .

because the bonding distance, the number, and the type of the neighboring atoms of the absorbing atoms are different depending whether they are residing at the core or on the shell. However, the difference in the atomic number between the Pt and Os is 2, and this minute value renders their L<sub>III</sub> absorption peaks (11,564 and 10,871 eV for the Pt and Os atoms, respectively) interfere with each other during XAS analysis. Hence, it is rather difficult to accurately determine the fitting parameters such as the coordination number ( $N$ ), the bond distance ( $R$ ), the Debye–Waller factor ( $\Delta\sigma_j^2$ ), and the inner potential shift ( $\Delta E_0$ ).

The DFT study of the Pt segregation on the Pt<sub>4</sub>Os slab is summarized in Fig. 6. The 5-layer 2 × 2 cell slab contains 16 Pt atoms and 4 Os atoms providing the 4:1 ratio. 4 Os atoms cannot be equally distributed in five layers so one of the layers should be pure Pt. The *a* slab shows a uniform Os distribution in four lower layers with the pure Pt top layer. This structure was chosen because from our previous calculations [52], we know that the Pt<sub>3</sub>Os alloy demonstrates strong surface segregation and the most stable Pt<sub>3</sub>Os slab structure has 100% Pt at the top surface layer, 50% Pt in the second layer, and 75% Pt in the following layer.

The *b* structure has pure Pt at the top and second layer but with 50% Os in the third layer and 25% Os in the following layers.

The *c* structure has also top two layers of Pt but with Os enriched in the bottom layer rather than in the third layer.

Our calculation shows that the most stable structure is *b*, followed by *a* and *c* (see Fig. 6). This is consistent with our previous segregation study of Pt-based binary alloys [52] which found that the most stable structure of the segregated alloys has Pt-skin on the surface. The 6-layer 2 × 2 and 4-layer 3 × 3 cell models provide a similar result. (see the Supporting information). Therefore, both experiment (STEM–EDS analysis) and theory (computational modeling) demonstrate that the DA–Pt<sub>2</sub>Os (Pt<sub>4</sub>Os) prefers the Pt-segregated surface structure. The Pt segregation is expected to influence the electronic structure of the alloy and affects its electrochemical activity, the main features of which will be described below.

Fig. 7 demonstrates the ORR CV curves in apparent current density for Pt<sub>2</sub>Os/C, DA–Pt<sub>2</sub>Os/C, and Pt/C. In the literatures, at potential below 0.6 V, the ORR response is under mass transport control limited by the diffusion of the dissolved oxygen in the electrolyte whereas at potential between 0.8 and 1 V, the ORR response is dominated by kinetics (the electrocatalytic activity of the electrocatalyst

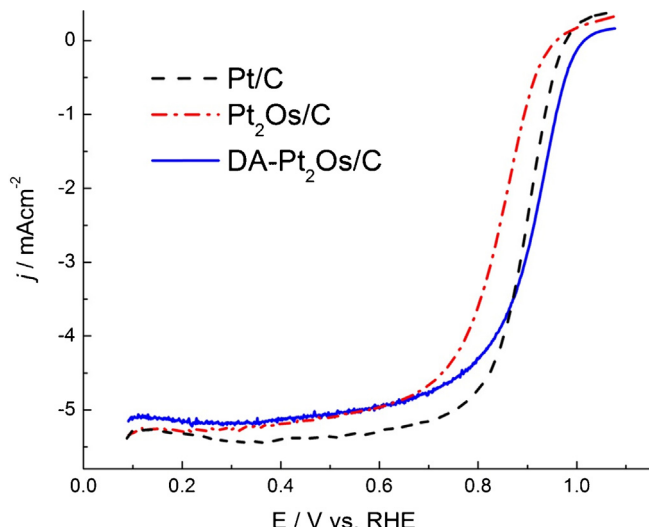


**Fig. 7.** The >ORR curves of Pt/C, Pt<sub>2</sub>Os/C, and DA–Pt<sub>2</sub>Os/C in apparent current density. The electrolyte was oxygen-saturated 0.1 M aqueous HClO<sub>4</sub> solution and the scan rate was 10 mV s<sup>-1</sup>.

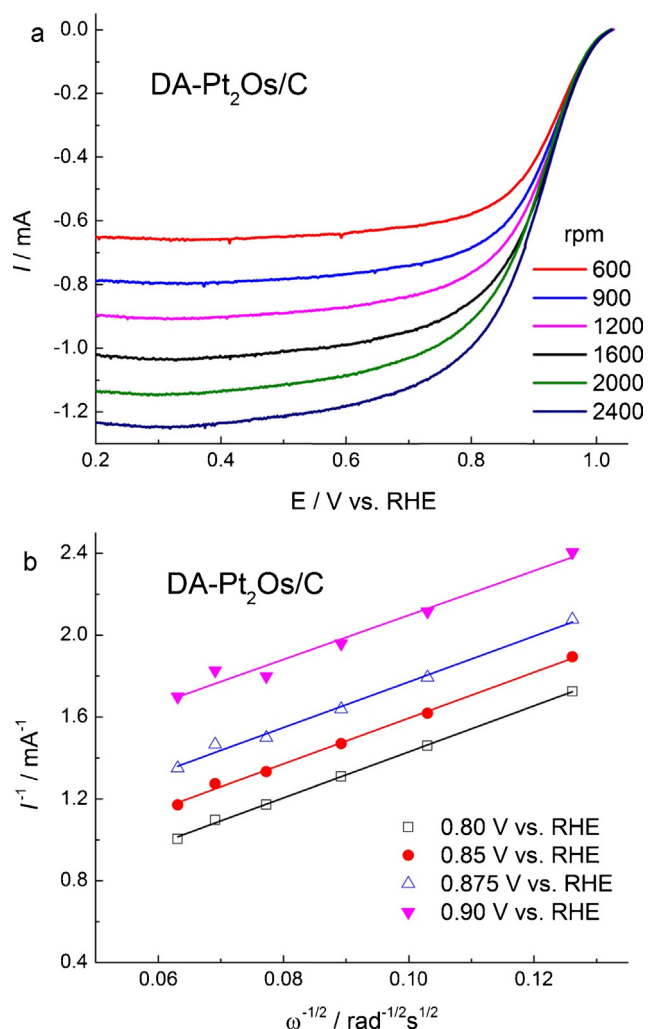


**Fig. 8.** (a) The >ORR curves of DA–Pt<sub>2</sub>Os/C at various rotation speeds. The electrolyte was oxygen-saturated 0.1 M aqueous HClO<sub>4</sub> solution and the scan rate was 10 mV s<sup>-1</sup>. (b) The Koutecky–Levich plot of DA–Pt<sub>2</sub>Os/C at different voltages.

involved in the ORR process) [76]. Hence, a simple method to quickly evaluate the ORR behavior of a potential electrocatalyst is the reading of half-wave potential, which is defined as the potential at which the magnitude of the current is half of the limiting current. In general, the larger the half-wave potential, the greater the ORR activity. As shown, the half-wave potentials for the Pt/C, Pt<sub>2</sub>Os/C, and DA–Pt<sub>2</sub>Os/C were 891, 837, and 908 mV, respectively. Moreover, the DA–Pt<sub>2</sub>Os/C exhibited the highest on-set potential of 1 V, and this provided another evidence of better electrocatalytic ability among these samples. It is also noted that the diffusion-limiting current for the Pt<sub>2</sub>Os/C and DA–Pt<sub>2</sub>Os/C at a rotation speed of 1600 rpm was 5.23 mA cm<sup>-2</sup>, a value that was rather close to that of Pt<sub>3</sub>Ni (5.36 mA cm<sup>-2</sup>) [77]. This consistency indicated that our ORR experiments were carried out properly.

Fig. 8a demonstrates the ORR curves from the DA–Pt<sub>2</sub>Os/C at various rotation speeds of RDE. Among these curves, the ORR responses at voltage below 0.6 V were stabilized at the limiting currents whose values were proportional to the rotation speed as expected. To extract the kinetic information, we employed the Koutecky–Levich equation listed below [78],

$$\begin{aligned} 1/i &= 1/i_{\text{kinetic}} + 1/i_{\text{diffusion limit}} \\ &= 1/i_{\text{kinetic}} + 1/0.62nFAD_{\text{O}_2}^{2/3}\omega^{1/2}v^{-1/6}\text{CO}_2 \end{aligned} \quad (1)$$

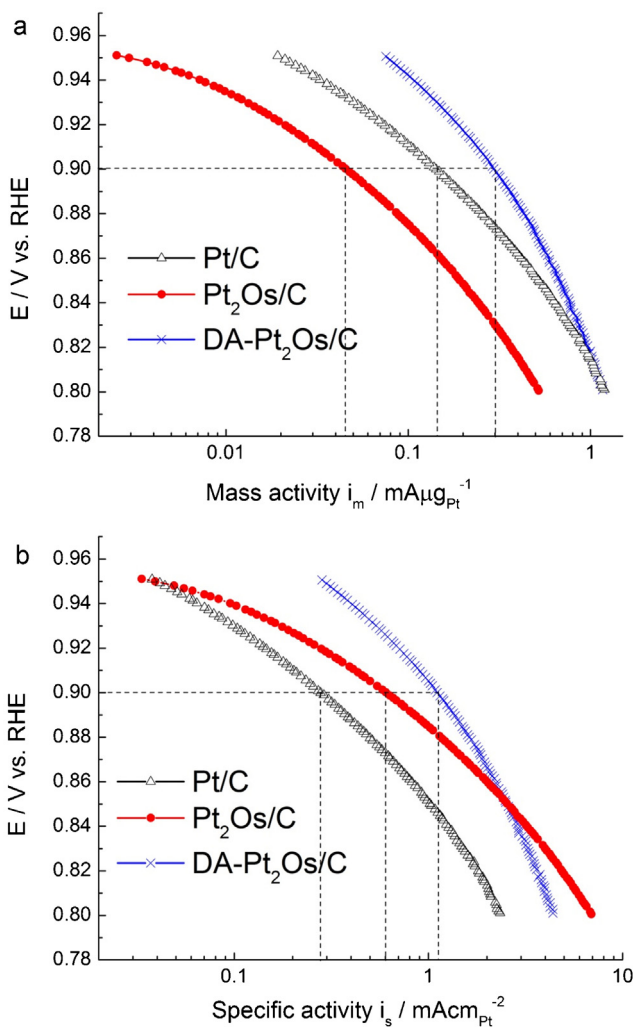


**Fig. 9.** The Tafel plots of the ORR curves (Fig. 5) in (a) mass activity and (b) specific activity.

where the  $i$  is the experimentally-measured current, the  $i_{\text{diffusion limit}}$  is the diffusion limiting current due to the limitation of mass transport of dissolved oxygen in the 0.1 M aqueous  $\text{HClO}_4$  solution, the  $i_{\text{kinetic}}$  is the kinetic current associated with the ORR activity of DA-Pt<sub>2</sub>Os/C, the  $n$  is the number of electron transferred in the ORR process, the  $F$  is the Faraday constant, the  $A$  is the reaction area of the RDE ( $0.196 \text{ cm}^2$ ), the  $D_{\text{O}_2}$  is the diffusivity of dissolved oxygen in the 0.1 M aqueous  $\text{HClO}_4$  solution ( $1.93 \times 10^{-5} \text{ cm}^2 \text{s}^{-1}$ ) [30], the  $\omega$  is the rotation speed of the RDE, the  $\nu$  is the kinematic viscosity of the 0.1 M aqueous  $\text{HClO}_4$  solution ( $1.009 \times 10^{-2} \text{ cm}^2 \text{s}^{-1}$ ) [79], and the  $C_{\text{O}_2}$  is the concentration of dissolved oxygen in the 0.1 M aqueous  $\text{HClO}_4$  solution ( $1.26 \times 10^{-3} \text{ mol L}^{-1}$ ) [30]. Fig. 8b provides the Koutecky–Levich plots at different potentials. Obviously, these curves showed a consistent pattern and the average slope was  $11.11 \text{ mA}^{-1} \text{ s}^{-1/2}$ . Thus, the resulting  $n$  value became 3.94. Therefore, we concluded that the DA-Pt<sub>2</sub>Os/C nanoparticles adopted a four-electron route to catalyze the ORR process, similar to that of Pt.

The values of  $i_{\text{kinetic}}$  obtained from the Koutecky–Levich equation were used to calculate the mass activity and specific activity shown in Fig. 9. These Tafel plots were obtained using  $i_{\text{kinetic}}$  values from 0.95 to 0.8 V divided by the effective mass of the Pt in the RDE (from ICP-MS) and ECSA ( $\text{cm}_{\text{Pt}}^{-2}$ ) values (from Fig. 3). For the Pt/C, its mass activity and specific activity at 0.9 V were  $0.14 \text{ mA} \mu\text{g}_{\text{Pt}}^{-1}$  and  $0.28 \text{ mA} \text{cm}_{\text{Pt}}^{-2}$ , respectively. These values

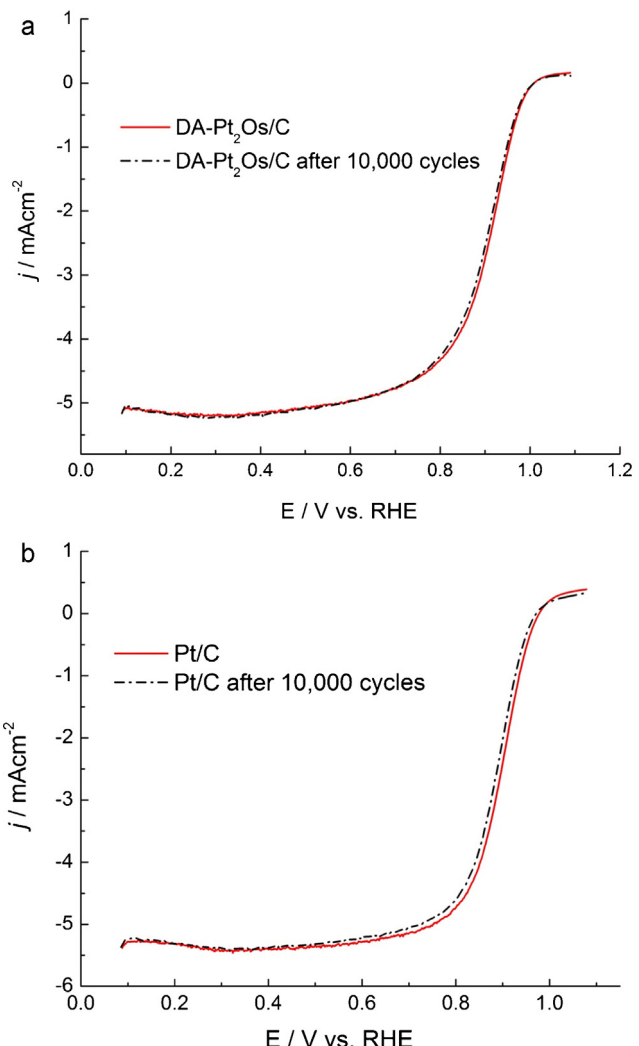


**Fig. 10.** The ORR curves before and after the durability test for (a) DA-Pt<sub>2</sub>Os/C and (b) Pt/C. The electrolyte was oxygen-saturated 0.1 M aqueous  $\text{HClO}_4$  solution and the scan rate was  $10 \text{ mV s}^{-1}$ .

were comparable to what were reported in the literatures for the Pt nanoparticles in similar sizes [80]. However, the Pt<sub>2</sub>Os/C exhibited a lower mass activity ( $0.05 \text{ mA} \mu\text{g}_{\text{Pt}}^{-1}$ ) and a greater specific activity ( $0.52 \text{ mA} \text{cm}_{\text{Pt}}^{-2}$ ), as compared to those of Pt/C. The reduced mass activity is attributed to its relatively larger size as compared to that of Pt/C because the predominant share of the Pt atoms was residing at the core. However, the 250% increment in the specific activity suggested the complementary role of Os atoms to the Pt atoms for ORR activity. This is because the surface of the Pt<sub>2</sub>Os nanoparticle was partially occupied by the Os atoms and those Os atoms were oxyphilic and thus promote the ORR process via bifunctional model and electronic mechanism. In the bifunctional model, the Os atoms exhibit a strong affinity toward the adsorption of OH and as a result, leads to a considerable reduction in the Pt-OH coverage [54]. In general, a larger percentage of OH coverage on the Pt sites is considered disadvantageous for the ORR action. According to Zhang et al., two OH species can adsorb onto a single Os atom and subsequently, initiates a spontaneous breakup of the O-H bonding forming an oxygen atom and water [54].

Once the dealloying process was completed, the DA-Pt<sub>2</sub>Os demonstrated a significantly-enhanced mass activity ( $0.29 \text{ mA} \mu\text{g}_{\text{Pt}}^{-1}$ ) and specific activity ( $1.03 \text{ mA} \text{cm}_{\text{Pt}}^{-2}$ ). We realized that the removal of Os atoms engendered a Pt-enriched surface with a substantially-enlarged ECSA. This surface-roughening

behavior has been reported in the literatures for dealloying treatments [53,81,82]. At this stage, the contributory role played by the Os atoms can be explained mostly by the electronic effect because the electronic structure of the surface Pt atoms was expected to be altered by the Os atoms underneath. It is noted that the mass activity and specific activity of DA-Pt<sub>2</sub>Os/C were comparable to other prominent binary nanoparticles such as PtNi and PtCo. In specific activity, the DA-Pt<sub>2</sub>Os/C demonstrated a greater value over those of cubic Pt<sub>3</sub>Ni nanoparticles ( $0.51 \text{ mA cm}_{\text{Pt}}^{-2}$ ) [28], activated Pt<sub>3</sub>Ni nanoparticles ( $0.65 \text{ mA cm}_{\text{Pt}}^{-2}$ ) [27], and octahedral Pt<sub>3</sub>Ni nanoparticles ( $0.85 \text{ mA cm}_{\text{Pt}}^{-2}$ ) [29], but lower than those of acid-treated Pt<sub>3</sub>Co nanoparticles after 1000 K heat treatment ( $1.4 \text{ mA cm}_{\text{Pt}}^{-2}$ ) [30], and ordered intermetallic Pt<sub>3</sub>Co nanoparticles ( $1.1 \text{ mA cm}_{\text{Pt}}^{-2}$ ) [35]. In mass activity, the DA-Pt<sub>2</sub>Os/C exhibited comparable values to those of cubic Pt<sub>3</sub>Ni nanoparticles ( $0.3 \text{ mA } \mu\text{g}_{\text{Pt}}^{-1}$ ) [28], activated Pt<sub>3</sub>Ni-sono nanoparticles ( $0.33 \text{ mA } \mu\text{g}_{\text{Pt}}^{-1}$ ) [27] acid-treated Pt<sub>3</sub>Co nanoparticles after 1000 K heat treatment ( $0.35 \text{ mA } \mu\text{g}_{\text{Pt}}^{-1}$ ) [30], and ordered intermetallic Pt<sub>3</sub>Co nanoparticles ( $0.31 \text{ mA } \mu\text{g}_{\text{Pt}}^{-1}$ ) [35], but lower than that of octahedral Pt<sub>3</sub>Ni nanoparticles ( $0.53 \text{ mA } \mu\text{g}_{\text{Pt}}^{-1}$ ) [29]. These results suggested that the DA-Pt<sub>2</sub>Os/C sample is a promising electrocatalyst for ORR and more engineering work to modify its surface state and morphology might lead to further enhancements in specific and mass activities.

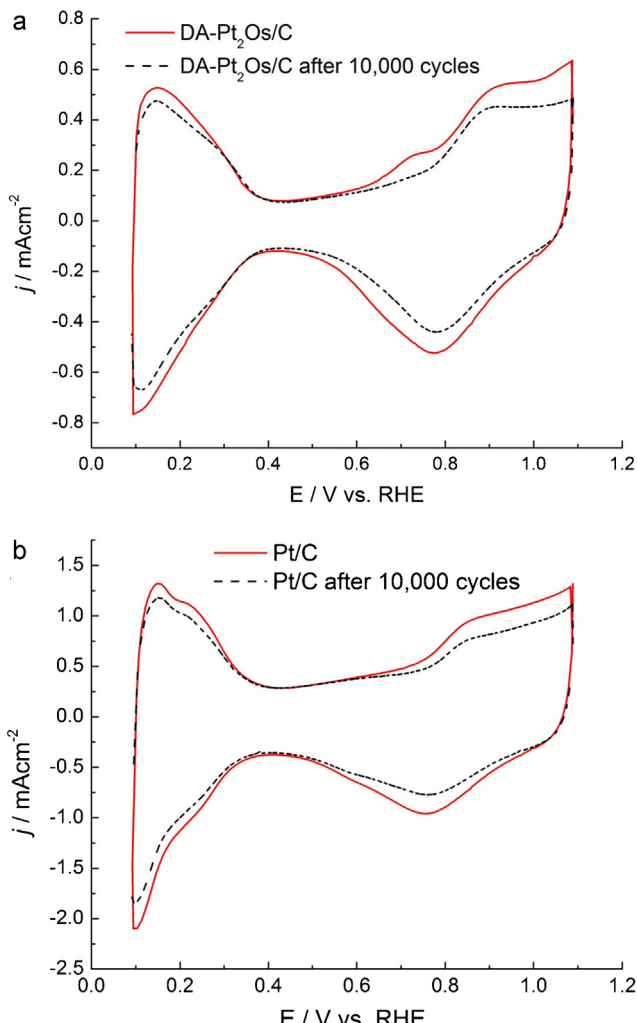


**Fig. 11.** The CV curves of (a) DA-Pt<sub>2</sub>Os/C and (b) Pt/C in deaerated 0.1 M aqueous HClO<sub>4</sub> solution at a scan rate of 50 mV s<sup>-1</sup>. These curves were used to determine the ECSA (highlighted area) before and after the durability test.

For durability tests, the DA-Pt<sub>2</sub>Os and Pt/C samples were subjected to multiple CV scans in a potential window of 0.65 and 1.05 V at 50 mV s<sup>-1</sup> in a 0.1 M aqueous HClO<sub>4</sub> solution following procedures used by Wang et al. [24]. Fig. 10 shows the ORR responses before and after the durability test for DA-Pt<sub>2</sub>Os/C and Pt/C, a and b, respectively. Apparently, for both samples there appeared a very subdued degradation during the durability tests, and both the onset potentials and diffusion-limiting currents remained almost unchanged. The minor degradation is manifested in the slight negative shift of the half-wave potential at 5 and 9 mV for DA-Pt<sub>2</sub>Os/C and Pt/C, respectively. These CV curves suggested that the stability of DA-Pt<sub>2</sub>Os/C was comparable or even better than that of commercially available Pt nanoparticles.

To further validate the stability of the DA-Pt<sub>2</sub>Os/C and Pt/C, we carried out the ECSA measurements before and after the durability tests, and the resulting CV curves are exhibited in Fig. 11. After the durability tests, the ECSA of DA-Pt<sub>2</sub>Os/C was reduced by 10.9% (from  $1.46 \text{ to } 1.3 \text{ cm}_{\text{Pt}}^2$ ), and a loss of 11.1% in the mass activity ( $0.27 \text{ to } 0.24 \text{ mA } \mu\text{g}_{\text{Pt}}^{-1}$ , assuming the Pt loading remained constant and the loss was attributed to the minor reduction of  $i_{\text{kinetic}}$  at 0.9 V from Fig. 10) was observed. In contrast, the Pt/C revealed a loss of 14.7% in the ECSA (from  $3.06 \text{ to } 2.61 \text{ cm}_{\text{Pt}}^2$ ) and a loss of 24.64% in the mass activity ( $0.142 \text{ to } 0.107 \text{ mA } \mu\text{g}_{\text{Pt}}^{-1}$ ). Clearly, the DA-Pt<sub>2</sub>Os/C revealed a better durability for the ORR. For both samples, we believed there was negligible physical detachment of electrocatalysts from the RDE during the durability tests because the diffusion-limiting currents remained unchanged. Therefore, the slight variation in the CV profiles was attributed to the aggregation of electrocatalysts that reduced the ECSA. The aggregation effect was also responsible for the moderate decrease of anodic currents at voltage above 0.85 V. It is noted that the impressive stability in life time tests is consistent with our QM calculation that confirmed the structural integrity of the DA-Pt<sub>2</sub>Os/C (Pt<sub>4</sub>Os) nanoparticles.

However, we would like to point out that the size of nanoparticles might be a factor in the durability tests. According to Xu et al., the Pt/C with larger nanoparticle sizes demonstrated better durability as compared to the sample with smaller nanoparticle sizes [83]. Indeed, in our case, the nanoparticle size of DA-Pt<sub>2</sub>Os was larger than that of commercial Pt/C. Therefore, it is possible that the size effect might also contribute to the enhanced durability for the DA-Pt<sub>2</sub>Os.

#### 4. Conclusions

We fabricated carbon-supported Pt<sub>2</sub>Os nanoparticles from a wet chemical reflux process and conducted a dealloying treatment in which the as-synthesized Pt<sub>2</sub>O/C underwent multiple CV scans to dissolve the Os atoms selectively from the surface of the Pt<sub>2</sub>Os nanoparticles. XRD diffraction signals from the dealloyed sample indicated a fcc phase and composition analysis suggested Pt<sub>4</sub>Os. Line scans from the STEM confirmed that the surface of Pt<sub>4</sub>Os was depleted with the Os atoms. The dealloyed sample revealed better ORR electrocatalytic activities ( $0.29 \text{ mA } \mu\text{g}_{\text{Pt}}^{-1}$  in mass activity and  $1.03 \text{ mA cm}_{\text{Pt}}^{-2}$  in specific activity), as compared to commercially available Pt/C and as-synthesized Pt<sub>2</sub>Os. In stability test, the dealloyed sample demonstrated impressive retention in the catalytic activities and smaller loss of ECSA as compared to those of Pt/C. In addition, we verified experimentally that the ORR steps occurring on the dealloyed sample is a four-electron process. The result of our DFT calculations on the DA-Pt<sub>2</sub>Os (Pt<sub>4</sub>Os) system is consistent with the STEM-EDS analysis and indicates a surface enrichment with Pt.

## Acknowledgments

The financial supports from the National Science Council of Taiwan (NSC-100-2221-E-009-075-MY3, NSC 101-3113-P-008 -001) and National Science Foundation (CBET-1067848, Caltech) are gratefully acknowledged.

## Appendix A. Supplementary data

Supplementary material related to this article can be found, in the online version, at <http://dx.doi.org/10.1016/j.apcatb.2014.01.004>.

## References

- [1] X. Li, Principles of Fuel Cells, Taylor & Francis, New York, NY, 2006.
- [2] R. O'Hayre, S.-W. Cha, W. Colella, F.B. Prinz, Fuel Cell Fundamentals, Wiley, New York, NY, 2006.
- [3] A.J. Appleby, F.R. Foulkes, Fuel Cell Handbook, Van Nostrand Reinhold, 1989.
- [4] K. Kordesch, G.R. Simader, Fuel Cells and Their Applications, VCH, New York, NY, 1996.
- [5] N.P. Brandon, S. Skinner, B.C.H. Steele, Annual Review of Materials Research 33 (2003) 183–213.
- [6] V. Mehta, J.S. Cooper, Journal of Power Sources 114 (2003) 32–53.
- [7] V.R. Stamenkovic, B. Fowler, B.S. Mun, G. Wang, P.N. Ross, C.A. Lucas, N.M. Markovic, Science 315 (2007) 493–497.
- [8] L.M. Vraca, D.B. Sepa, A. Damjanovic, Journal of The Electrochemical Society 133 (1986) 1835–1839.
- [9] C.-L. Lee, H.-P. Chiou, Applied Catalysis B: Environmental 117–118 (2012) 204–211.
- [10] R. Jasinski, Nature 201 (1964) 1212–1213.
- [11] D. Nguyen-Thanh, A.I. Frenkel, J. Wang, S. O'Brien, D.L. Akins, Applied Catalysis B: Environmental 105 (2011) 50–60.
- [12] J. Zagal, F. Bediouji, J. Dodelet, N4-Macrocyclic Metal Complexes, Springer, 2006.
- [13] H. Jahnke, M. Schönborn, G. Zimmermann, in: F.P. Schäfer, H. Gerischer, F. Willig, H. Meier, H. Jahnke, M. Schönborn, G. Zimmermann (Eds.), Physical and Chemical Applications of Dyestuffs, Springer, Berlin Heidelberg, 1976, pp. 133–181.
- [14] Y.-g. Wang, Y.-y. Xia, Electrochemistry Communications 8 (2006) 1775–1778.
- [15] J.-H. Kim, A. Ishihara, S. Mitsushima, N. Kamiya, K.-I. Ota, Electrochimica Acta 52 (2007) 2492–2497.
- [16] K. Lee, L. Zhang, J. Zhang, Electrochemistry Communications 9 (2007) 1704–1708.
- [17] H. Behret, H. Binder, G. Sandstede, Electrochimica Acta 20 (1975) 111–117.
- [18] A. Morozan, B. Jousselme, S. Palacin, Energy & Environmental Science 4 (2011) 1238–1254.
- [19] D. Sebastián, I. Suelves, R. Moliner, M.J. Lázaro, A. Stassi, V. Baglio, A.S. Aricó, Applied Catalysis B: Environmental 132–133 (2013) 22–27.
- [20] T.S. Ahmad, Z.L. Wang, T.C. Green, A. Henglein, M.A. El-Sayed, Science 272 (1996) 1924–1925.
- [21] J. Chen, B. Lim, E.P. Lee, Y. Xia, Nano Today 4 (2009) 81–95.
- [22] Z. Peng, H. Yang, Nano Today 4 (2009) 143–164.
- [23] Y. Chen, J. Xu, X. Liu, Y. Tang, T. Lu, Applied Catalysis B: Environmental 140–141 (2013) 552–558.
- [24] J.X. Wang, C. Ma, Y. Choi, D. Su, Y. Zhu, Y. Zhu, R. Si, M.B. Vukmirovic, Y. Zhang, R.R. Adzic, Journal of the American Chemical Society 133 (2011) 13551–13557.
- [25] D.A. Cantane, F.E.R. Oliveira, S.F. Santos, F.H.B. Lima, Applied Catalysis B: Environmental 136–137 (2013) 351–360.
- [26] H.-Y. Park, T.-Y. Jeon, J.H. Jang, S.J. Yoo, K.-H. Choi, N. Jung, Y.-H. Chung, M. Ahn, Y.-H. Cho, K.-S. Lee, Y.-E. Sung, Applied Catalysis B: Environmental 129 (2013) 375–381.
- [27] C. Gümeci, Z. Li, D.J.C. Jr., C. Korzeniewski, Journal of The Electrochemical Society 159 (2012) F35–F41.
- [28] J. Zhang, H. Yang, J. Fang, S. Zou, Nano Letters 10 (2010) 638–644.
- [29] J. Wu, J. Zhang, Z. Peng, S. Yang, F.T. Wagner, H. Yang, Journal of the American Chemical Society 132 (2010) 4984–4985.
- [30] S. Chen, W. Sheng, N. Yabuuchi, P.J. Ferreira, L.F. Allard, Y. Shao-Horn, The Journal of Physical Chemistry C 113 (2009) 1109–1125.
- [31] V.R. Stamenkovic, B.S. Mun, M. Arenz, K.J.J. Mayrhofer, C.A. Lucas, G. Wang, P.N. Ross, N.M. Markovic, Nature Materials 6 (2007) 241–246.
- [32] S. Koh, C. Yu, P. Mani, R. Srivastava, P. Strasser, Journal of Power Sources 172 (2007) 50–56.
- [33] T. Toda, H. Igarashi, M. Watanabe, Journal of Electroanalytical Chemistry 460 (1999) 258–262.
- [34] H.A. Gasteiger, S.S. Kocha, B. Sompalli, F.T. Wagner, Applied Catalysis B: Environmental 56 (2005) 9–35.
- [35] D. Wang, H.L. Xin, R. Hovden, Hongsen Wang, Y. Yu, D.A. Muller, F.J. DiSalvo, H.D. Abruna, Nature Materials 12 (2012) 81–87.
- [36] R.R. Adzic, J. Zhang, K. Sasaki, M.B. Vukmirovic, M. Shao, J.X. Wang, A.U. Nilekar, M. Mavrikakis, J.A. Valerio, F. Uribe, Topics in Catalysis 46 (2007) 249–262.
- [37] J. Zhang, K. Sasaki, E. Sutter, R.R. Adzic, Science 315 (2007) 220–222.
- [38] P. Strasser, S. Koh, T. Anniyev, J. Greeley, K. More, C. Yu, Z. Liu, S. Kaya, D. Nordlund, H. Ogasawara, M.F. Toney, A. Nilsson, Nature Chemistry 2 (2010) 454–460.
- [39] P. Mani, R. Srivastava, P. Strasser, Journal of Power Sources 196 (2011) 666–673.
- [40] L. Gan, M. Heggen, S. Rudi, P. Strasser, Nano Letters 12 (2012) 5423–5430.
- [41] C. Cui, L. Gan, M. Heggen, S. Rudi, P. Strasser, Nature Materials 12 (2013) 765–771.
- [42] M. Oezaslan, M. Heggen, P. Strasser, Journal of the American Chemical Society 134 (2011) 514–524.
- [43] R. Srivastava, P. Mani, N. Hahn, P. Strasser, Angewandte Chemie International Edition 46 (2007) 8988–8991.
- [44] M. Oezaslan, F. Hasché, P. Strasser, Journal of The Electrochemical Society 159 (2012) B394–B405.
- [45] M. Oezaslan, F. Hasché, P. Strasser, Journal of The Electrochemical Society 159 (2012) B444–B454.
- [46] J. Kua, W.A. Goddard, Journal of the American Chemical Society 121 (1999) 10928–10941.
- [47] K.L. Ley, R. Liu, C. Pu, Q. Fan, N. Leyarovska, C. Segre, E.S. Smotkin, Journal of The Electrochemical Society 144 (1997) 1543–1548.
- [48] Y. Zhu, C.R. Cabrera, Electrochemical and Solid-State Letters 4 (2001) A45–A48.
- [49] B. Gurau, R. Viswanathan, R. Liu, T.J. Lafrenz, K.L. Ley, E.S. Smotkin, E. Reddington, A. Sapienza, B.C. Chan, T.E. Mallouk, S. Sarangapani, The Journal of Physical Chemistry B 102 (1998) 9997–10003.
- [50] R. Liu, H. Iddir, Q. Fan, G. Hou, A. Bo, K.L. Ley, E.S. Smotkin, Y.E. Sung, H. Kim, S. Thomas, A. Wieckowski, The Journal of Physical Chemistry B 104 (2000) 3518–3531.
- [51] J. Kim, S. Kim, C.K. Rhee, Langmuir 27 (2011) 2044–2051.
- [52] T.H. Yu, Y. Sha, B.V. Merinov, W.A. Goddard III, The Journal of Physical Chemistry C 114 (2010) 11527–11533.
- [53] V.R. Stamenkovic, B.S. Mun, K.J.J. Mayrhofer, P.N. Ross, N.M. Markovic, Journal of the American Chemical Society 128 (2006) 8813–8819.
- [54] J. Zhang, M.B. Vukmirovic, K. Sasaki, A.U. Nilekar, M. Mavrikakis, R.R. Adzic, Journal of the American Chemical Society 127 (2005) 12480–12481.
- [55] K. Kinoshita, P. Stonehart, in: J.O.M. Bockris, B.E. Conway (Eds.), Modern Aspects of Electrochemistry, Springer, US, 1977, pp. 183–266.
- [56] F. Gloaguen, J.M. Le'Ger, C. Lamy, Journal of Applied Electrochemistry 27 (1997) 1052–1060.
- [57] Y.C. Hsieh, L.C. Chang, P.W. Wu, Y.M. Chang, J.F. Lee, Applied Catalysis B: Environmental 103 (2011) 116–127.
- [58] P. Schultz, Sandia National Laboratories (<http://www.cs.sandia.gov/~paschl/Quest/>) (2009).
- [59] J.P. Perdew, K. Burke, M. Ernzerhof, Physical Review Letters 77 (1996) 3865–3868.
- [60] J.P. Perdew, A. Zunger, Physical Review B: Condensed Matter 23 (1981) 5048–5079.
- [61] C.F. Melius, W.A. Goddard III, Physical Review A: Atomic, Molecular, and Optical Physics 10 (1974) 1528–1540.
- [62] C.F. Melius, B.D. Olafson, W.A. Goddard III, Chemical Physics Letters 28 (1974) 457–462.
- [63] A. Redondo, W.A. Goddard III, T.C. McGill, Physical Review B: Condensed Matter 15 (1977) 5038–5048.
- [64] D.R. Hamann, Physical Review B: Condensed Matter 40 (1989) 2980–2987.
- [65] J. Huang, H. Yang, Q. Huang, Y. Tang, T. Lu, D.L. Akins, Journal of The Electrochemical Society 151 (2004) A1810–A1815.
- [66] D. Wang, P. Zhao, Y. Li, Scientific Reports, doi:10.1038/srep00037.
- [67] J. Xu, Y. Wang, Z. Zhang, The Journal of Physical Chemistry C 116 (2012) 5689–5699.
- [68] Y. Sun, T.J. Balk, Scripta Materialia 58 (2008) 727–730.
- [69] S. Koh, P. Strasser, Journal of The American Chemical Society 129 (2007) 12624–12625.
- [70] R. Yang, J. Leisch, P. Strasser, M.F. Toney, Chemistry of Materials 22 (2010) 4712–4720.
- [71] J.T. Moore, D. Chu, R. Jiang, G.A. Deluga, C.M. Lukehart, Chemistry of Materials 15 (2003) 1119–1124.
- [72] G. Orozco, C. Gutie'rez, Journal of Electroanalytical Chemistry 484 (2000) 64–72.
- [73] N. Kolpakova, L. Shvets, A. Stromberg, Soviet Electrochemistry 28 (1992) 592–600.
- [74] J.E. Greedan, D.B. Willson, T.E. Haas, Inorganic Chemistry 7 (1968) 2461–2463.
- [75] C.K. Rhee, M. Wakisaka, Y.V. Tolmachev, C.M. Johnston, R. Haasch, K. Attenkofer, G.Q. Lu, H. You, A. Wieckowski, Journal of Electroanalytical Chemistry 554–555 (2003) 367–378.
- [76] U.A. Paulus, T.J. Schmidt, H.A. Gasteiger, R.J. Behm, Journal of Electroanalytical Chemistry 495 (2001) 134–145.
- [77] U.A. Paulus, A. Wokaun, G.G. Scherer, T.J. Schmidt, V. Stamenkovic, V. Radmilovic, N.M. Markovic, P.N. Ross, The Journal of Physical Chemistry B 106 (2002) 4181–4191.
- [78] A. Bard, L. Faulkner, Electrochemical Methods: Fundamentals and Applications, John Wiley & Sons, Inc, Hoboken NJ, USA, 2001.

- [79] N.M. Markovic, H.A. Gasteiger, P.N. Ross, *The Journal of Physical Chemistry* 99 (1995) 3411–3415.
- [80] B. Lim, M. Jiang, P.H.C. Camargo, E.C. Cho, J. Tao, X. Lu, Y. Zhu, Y. Xia, *Science* 324 (2009) 1302–1305.
- [81] C. Wang, M. Chi, D. Li, D. Strmcnik, D. van der Vliet, G. Wang, V. Komanicky, K.-C. Chang, A.P. Paulikas, D. Tripkovic, J. Pearson, K.L. More, N.M. Markovic, V.R. Stamenkovic, *Journal of the American Chemical Society* 133 (2011) 14396–14403.
- [82] K.T. Kim, Y.G. Kim, J.S. Chung, *Journal of The Electrochemical Society* 142 (1995) 1531–1539.
- [83] Z. Xu, H. Zhang, H. Zhong, Q. Lu, Y. Wang, D. Su, *Applied Catalysis B: Environmental* 111–112 (2012) 264–270.